Receptivity of Hypersonic Boundary Layers to Distributed Roughness and Acoustic Disturbances

P. Balakumar

Flow Physics and Control Branch
NASA Langley Research Center, Hampton, VA 23681

Boundary-layer receptivity and stability of Mach 6 flows over smooth and rough seven-degree half-angle sharp-tipped cones are numerically investigated. The receptivity of the boundary layer to slow acoustic disturbances, fast acoustic disturbances, and vortical disturbances is considered. The effects of three-dimensional isolated roughness on the receptivity and stability are also simulated. The results for the smooth cone show that the instability waves are generated in the leading edge region and that the boundary layer is much more receptive to slow acoustic waves than to the fast acoustic waves. Vortical disturbances also generate unstable second modes, however the receptivity coefficients are smaller than that of the slow acoustic wave. Distributed roughness elements located near the nose region decreased the receptivity of the second mode generated by the slow acoustic wave by a small amount. Roughness elements distributed across the continuous spectrum increased the receptivity of the second mode generated by the slow and fast acoustic waves and the vorticity wave. The largest increase occurred for the vorticity wave. Roughness elements distributed across the synchronization point did not change the receptivity of the second modes generated by the acoustic waves. The receptivity of the second mode generated by the vorticity wave increased in this case, but the increase is lower than that occurred with the roughness elements located across the continuous spectrum. The simulations with an isolated roughness element showed that the second mode waves generated by the acoustic disturbances are not influenced by the small roughness element. Due to the interaction, a three-dimensional wave is generated. However, the amplitude is orders of magnitude smaller than the two-dimensional wave.

I. Introduction

TRANSITION in two-dimensional hypersonic boundary layers in quiet environments is generally caused by second-mode (Mack's mode)[1] disturbances. These modes originate due to the appearance of a supersonic region relative to the disturbance phase velocity. Numerical, experimental, and theoretical investigations have been performed to understand these instability modes for hypersonic boundary layers.[1-19] Figure 1 displays a typical linear stability diagram for a hypersonic boundary layer for a single frequency. Figure 1(a) shows the evolution of phase speed c_r and the growth rate $-\alpha_i$, and Fig. 1(b) shows the wavenumber α_r and the wavelength. These results are shown for a hypersonic flow over a cone with a half-angle of 7 degrees at a free stream Mach number of $M = 6$. In hypersonic boundary layers, among all the discrete modes, the slow and the fast modes are the two relevant modes for boundary layer transition[12, 13]. The slow and the fast modes correspond to the discrete modes whose phase speeds approach the phase speeds of the slow and the fast acoustic wave, *1-1/M* and *1+1/M*, respectively, as the Reynolds number decreases towards zero. As the Reynolds number increases, the phase speed of the slow mode increases gradually from *1-1/M* to 1.0 and the phase speed of the fast mode decreases gradually from *1+1/M* to 1.0. As the phase speed of the fast mode approaches 1.0, the fast mode is absorbed into the continuous spectrum (solid line). Downstream of this point, a new mode with slightly different eigenvalues and eigenfunctions springs from the continuous spectrum. Although there is a discontinuity in the eigenvalues and eigenfunctions across the continuous spectrum, the new mode is still referred to as the fast mode. Further downstream, the phase speed of the fast mode continues to decrease and at some point the phase speeds of the slow, and the fast modes cross each other. This point is termed as the synchronization point (dotted line).

Hence, we identify three different regions that may be more receptive to external disturbances such as acoustic, turbulence, and roughness in generating unstable disturbances inside the boundary layer. One is the region very close to the leading edge or the nose region where the slow and the fast acoustic disturbances in the free stream

could synchronize efficiently with the slow and the fast instability modes of the boundary layer. The second is the continuous spectrum region where the disturbances such as turbulence and entropy that are convecting with the free stream velocity could interact with the boundary layer and excite instability waves inside the boundary layer. The third is the synchronization region where the approaching slow and the fast modes pass through the synchronization point and emerge as slow and fast instability modes with different amplitudes.

In previous work by the current author and his colleagues,[20-26] the interactions of slow and fast acoustic waves, and vorticity waves with hypersonic boundary layers over smooth sharp and blunt flat plates, wedges, and cones were investigated. The results showed that the slow and the fast acoustic waves synchronized with the slow and the fast discrete modes near the leading edge or the nose region. In the adiabatic wall case, the slow mode continues to grow exponentially downstream. The receptivity coefficient of the slow discrete mode is about 5 to 10 times the amplitude of the forced slow acoustic wave. The amplitude of the fast mode evolves as predicted by the stability theory until the continuous spectrum and the synchronization point region and hooks onto the unstable second mode downstream. The amplitude of the fast discrete mode is about 20 times smaller than that for the slow acoustic mode. The disturbances generated by the vortical disturbances evolve downstream and transform into the unstable second mode near the continuous spectrum region. The amplitude of the unstable second mode in this case is about 5 times smaller than that for the slow acoustic wave.

In addition to investigating transition on smooth surfaces, many researchers have been studying how roughness affects the transition in hypersonic boundary layers. Reda[27] and Schneider[28] reviewed the roughness-induced transition in hypersonic boundary layers. The surface roughness is characterized as either two-dimensional or three-dimensional, and either isolated or distributed. In addition to these global characteristics, local characteristics such as height, shape, and location of the roughness also influence the transition. Holloway et al.[29] and Fujii[30] experimentally observed that two-dimensional isolated roughness and a wavy wall delayed transition at hypersonic Mach numbers. Recently, Marxen et al.[31] numerically investigated the disturbance amplification in a Mach 4.8 flat plate boundary layer with localized two-dimensional roughness elements of different heights. Unsteady perturbations at a fixed frequency were generated by blowing and suction at the wall upstream of the roughness. They conclude that a two-dimensional roughness element acts like an amplifier capable of amplifying some frequency range and damping others. Bountin et al.[32] investigated experimentally and numerically the control of the second mode waves using a spanwise corrugated surface at a Mach number of 6. The results showed that the separation bubbles formed between the grooves stabilize the growth of the second modes. In their simulation, the unsteady perturbations are also introduced by the blowing and suction on the wall. However, questions remain about the role of the roughness in the generation and growth of the second modes generated by the free stream disturbances. Does the roughness affect the receptivity process of the second modes generated by the free stream acoustic and vortical disturbances and/or does the roughness modify the boundary layer downstream and hence modify the stability characteristics? The work presented in this paper is aimed at answering these questions.

The focus of this paper is on the effects of two and three-dimensional isolated and distributed roughness on the generation and evolution of second mode disturbances in hypersonic boundary layers. The effects of isolated and distributed roughness located near the nose region of a hypersonic boundary layer over a 7° half-angle sharp-tipped cone at a free stream Mach number of 6 have been investigated in Ref. (33). This paper presents an investigation into the effects of two-dimensional distributed roughness located across the continuous spectrum and across the synchronization point. First, the disturbance field generated by the interaction of free stream slow acoustic waves, fast acoustic waves, and vorticity waves with the smooth cone is simulated. Then, rectangular shaped two-dimensional distributed roughness is placed near the nose region, across the continuous spectrum region, and across the synchronization point and simulations were performed to study the effects of the roughness on the receptivity and the stability. After identifying the effects of the roughness locations on the receptivity, the extent and location of the roughness was varied to identify the most receptive locations. Finally, the effects of isolated three-dimensional roughness elements, with periodic boundary conditions in the azimuthal direction, on the generation of instability waves by free stream slow acoustic disturbances are investigated.

II. Models and Flow Conditions

The model is a 7° half-angle sharp-tipped cone with a nose radius of 0.015 mm (Fig. 2). Computations were performed for a freestream Mach number of 6. The freestream stagnation temperature and pressure were 433°K and 12.2 kPa (140 psi), yielding a unit Reynolds number of 10.4*10^6/m. The simulations were performed for a constant wall temperature of 300°K. The cone model geometry was tested in the Boeing/AFOSR Mach 6 Quiet Tunnel at the same freestream conditions.[9] The Sutherland viscosity law was used with a constant Prandtl number of 0.70. The

non-dimensional frequency F is defined as $F = \dfrac{2\pi v_\infty f}{U_\infty^2}$, where f is the frequency in hertz. For the above flow conditions, $F = 1*10^{-4}$ corresponds to a frequency of 144.23 kHz.

III.   Roughness

A. Two-dimensional Roughness

Two-dimensional rectangular roughness elements were placed on the surface of the cone at different locations along the cone. The shape of the roughness is in the form:

$$y_c(x) = \frac{h}{2}\sum_{n=1}^{N}\left[\tanh \sigma_x \frac{x - x_n}{\Delta x} - \tanh \sigma_x \frac{x - (x_n + w)}{\Delta x}\right]$$
$$x_n = x_0 + (n-1)*(2w)$$

(1)

Here y_c is the height of the roughness normal to the surface of the cone, h is the maximum height, x_o is the starting location of the roughness, w is the width of the roughness, and σ_x and Δx determine the streamwise spatial extent of the roughness near the edges. The spacing between two roughness elements in the simulations is two times the width of one roughness, and N is the number of roughness elements. Fig. 2(b) depicts the shape for a single roughness element and Fig. 2(c) shows the roughness distribution for multiple roughness elements. Simulations are performed for different widths, heights, locations, and number of roughness elements.

B. Three-dimensional Roughness

Three-dimensional cubic roughness elements are placed periodically in the azimuthal direction as shown in Fig. 2(d) and (e). The number of elements in the azimuthal direction is m and the spacing between the elements are $2\pi/m$. The shape of a three-dimensional cubic roughness element is in the form

$$y_{3d}(x,\theta) = y_c(x)\left[\tanh \sigma_\theta \frac{\theta - \theta_0}{\Delta \theta} - \tanh \sigma_\theta \frac{\theta + \theta_0}{\Delta \theta}\right]$$

(2)

Here $y_{3d}(x,\theta)$ is the height of the roughness normal to the surface of the cone, $\theta_o = \pi/m$ is the starting location of the roughness in the azimuthal direction, and σ_θ and $\Delta\theta$ determine the azimuthal extent of the roughness near the edges. This roughness distribution mimics the steps and gaps presented by the surface tiles of a thermal protection system on a hypersonic vehicle.

IV.   Governing Equations

The three-dimensional unsteady compressible Navier-Stokes equations, written in conservation form and in cylindrical coordinates, are solved. The viscosity, μ, is computed using Sutherland's law and the coefficient of conductivity, k, is given in terms of a constant Prandtl number, $Pr = 0.7$. For the computation, the equations are transformed from the physical coordinate system (x, r, θ) to the computational curvilinear coordinate system (ξ, η, ς) in a conservative manner.

A. Solution Algorithm

The governing equations were solved using a 5th-order accurate weighted essentially non-oscillatory (WENO) scheme for space discretization and a 3rd-order total-variation-diminishing (TVD) Runge-Kutta scheme for time integration. The WENO and TVD methods and formulas are explained in Shu[34]. The application of the ENO method to the Navier-Stokes equations is presented by Atkins[35]. The solution method implemented in the present computations are described in Balakumar et al.[36].

We used body-fitted curvilinear grid system in all the simulations. The grid stretches in the η direction close to the wall and is uniform outside the boundary layer. In the ξ direction, the grid is symmetric about the nose and is very fine near the nose and becomes uniform in the flat region. The grid is uniform in the azimuthal ζ direction. The outer boundary outside of the shock follows a parabola where the vertex is located a short distance upstream of

American Institute of Aeronautics and Astronautics

the nose to capture the boundary layer accurately. Fig. 3(a-b) show the grid system employed for the flow over a three-dimensional roughness element. Figure 3a depicts the grid distribution in one (x, y) plane for $\theta = 0$ and Fig. 3b shows the body-fitted grid over the roughness in the azimuthal (y, θ) plane across the roughness. We used 251 points in the normal direction, 65 points in the azimuthal direction and a minimum of 20 points per wavelength in the streamwise direction.

V. Results

A. 7° Half-Angle Sharp-Tipped Cone Results for the Smooth-Wall Case

1. Mean Flow and Linear Stability for the Smooth-Wall Case

Figure 4(a) and (b) show the computed mean density contours for the sharp-tipped cone. The flow field for the entire computational domain is shown in Fig. 4(a), while Fig. 4(b) shows a close-up view of the nose region. The mean flow boundary layer profiles at different axial locations $x = 0.5, 3, 10, 20, 30$ and 50 cm are shown in Fig. 5. The boundary layer thickness increases from 0.20 mm at $x = 0.5$ cm. to 2.0 mm at $x = 50$ cm.

Figs. 1(a) and 1(b) show the evolution of the eigenvalues along the axial direction for the slow (Mode S) and fast (Mode F) modes for the frequency $F = 1.5*10^{-4}$ (217 kHz). Figure 1(a) shows the evolution of phase speed c_r and the growth rate $-\alpha_i$ and Fig. 1(b) shows the wavenumber α_r and the wavelength. As the fast mode evolves downstream, it merges with the continuous spectrum with phase speed $c_r = 1.0$. For this frequency of $F = 1.5*10^{-4}$ the merging occurs around $x = 281$ mm. Downstream of the continuous spectrum a new mode with slightly different eigenvalues and eigenfunctions emerges. These points are also marked as red dots in Fig. 1(a). As the slow mode and the new fast mode evolve downstream, the slow mode becomes the unstable Mack's second mode and the fast mode becomes the stable mode. The neutral point for the slow mode occurs at $x=275$ mm. The synchronization of the phase speeds for the slow and the fast modes occurs near $x = 360$ mm. The growth rates of the slow mode and the fast mode at this point are $-\alpha_i = 0.005$ and -0.02, respectively. The continuous spectrum and the synchronization point are also marked as vertical lines in Fig 1(a). This figure suggests that roughness located near the nose, the continuous spectrum location, and the synchronization region may influence the receptivity of the unstable second mode strongly.

Table 1 gives the wavenumbers and the wavelengths in dimensional and non-dimensional units for the slow and the fast acoustic waves, the vorticity waves, and for the neutral stability waves. It is interesting to see that in all the cases the wavelengths for the acoustic waves match with the wavelengths for the stability waves. The wavelengths of the slow and the fast acoustic waves at zero incidence at the frequency $F = 1.50*10^{-4}$ are 3.35 and 4.69 mm, and the wavelengths for the slow and the fast instability waves near the leading edge of the cone are 3.47 and 4.64 mm. The wavelengths of the vorticity waves do not match the wavelengths of either the slow or the fast modes. The wavelength of the vorticity wave is 4.02 mm, which lies in the middle of the wavelengths for the slow and the fast stability modes. Figure 6 shows the N-Factor variation for different frequencies obtained using parallel and non-parallel parabolized stability equations (PSE) methods. The maximum N-factor obtained is about 7.0 and the corresponding frequency is $F=1.5*10^{-4}$ (217 kHz).

Table 1: Values of α_{ac} and wavelength at the frequency of $F = 1.5*10^{-4}$.

θ_y	Slow acoustic	Fast acoustic	Vorticity	Cone (Stability) X=60mm	
				Slow	Fast
0	0.1835 (3.35 mm)	0.1310 (4.69 mm)	0.153 (4.02 mm)	0.1772 (3.47 mm)	0.1328 (4.64 mm)

2. Interaction of Slow and Fast Acoustic Waves and Vorticity Waves with the Smooth-Wall Cone

Detailed results for the interactions of slow acoustic waves, fast acoustic waves, and vorticity waves are given in a previous paper[26]. After the mean flow was computed, two-dimensional slow and fast acoustic disturbances and vorticity disturbances (with an amplitude of $\tilde{p}_{ac} / p_\infty = 1*10^{-5}$ for the acoustic waves and with an amplitude of $\tilde{u} / U_\infty = 1.0*10^{-5}$ for the vorticity waves) at an incidence angle of 0 degrees were introduced at the outer boundary of the computational domain and time-accurate simulations were performed. The results are presented for the most amplified frequency of $F = 1.5*10^{-4}$ (217 kHz).

Figures 7(a-c) show the amplitude of the pressure fluctuations along the surface of the cone for the slow and the fast acoustic waves and for the vorticity waves. Figure 7 also includes the results from the parabolized stability equations (PSE) computations obtained for the same mean boundary layer profiles. The figure for the slow wave clearly shows the initial generation and the eventual exponential growth of the instability waves inside the boundary layer. The slow acoustic wave whose wavelength (3.35 mm) is close to the wavelength of the slow mode (Mode S) near the leading edge (3.47 mm) transforms into instability waves rather directly. Similarly, the fast acoustic mode whose wavelength (4.69 mm) is close to the wavelength of the fast mode (Mode F) near the leading edge (4.64 mm) synchronizes with the instability mode near the leading edge region. As was observed in Fig. 1(a), the fast mode does not evolve into an unstable second mode as the Reynolds number increases. Figure 7(b) shows that as the disturbance induced by the fast mode evolves downstream it first grows up to $x \sim 12$ cm, then decreases and oscillates before it grows due to the second mode instability. The unstable second mode generated by the fast mode is weak compared to that generated by the slow mode. The maximum amplitude reached in the slow acoustic wave case is about 0.213 and it is about 0.0023 in the fast acoustic case. Simulations were also performed with axisymmetric vortical disturbances.[9] Figures 7(c) depicts the wall pressure fluctuations generated by the interaction of vortical disturbances with the cone. The results show that the disturbances grow up to $x \sim 30$ cm, then decrease to a minimum value close to $x = 33$ cm and increase downstream due to the second mode instability. The maximum amplitude obtained in this case is about 0.078. Table 2 summarizes the maximum amplitudes reached by the disturbances in different cases. The fast mode is about 93 times less efficient than the slow mode, and the vortical disturbance is about 2.7 times less efficient.

Table 2: Maximum amplitudes of pressure fluctuations for different cases F=1.5*10^{-4}

θ_y	Max. amplitude	Ratio = max/max$_{slow}$
0 *Slow*	0.213	1.0
0 *Fast*	0.0023	1/93
0 Vorticity	0.078	1/2.7

B. Results for the Rough Wall Cases

Steady and unsteady simulations were performed with isolated and distributed two and three-dimensional roughness elements placed at different axial locations to investigate the effects of small roughness elements on the receptivity and the stability of hypersonic boundary layers. The shapes of the roughness elements are given in eqs. (1) and (2).

1. Two-dimensional Roughness Cases

First we present the results for two-dimensional isolated and distributed roughness cases. Simulations are performed for several roughness heights and locations. Table 3 gives the roughness parameters for which the results are presented.

Table 3: Two-dimensional roughness locations and parameters for different cases

Case	X_0 (mm)	N	w (mm)	h(mm)	h/δ	Re_{kk}
1	5	1	1.25	0.05	1/4	13
2	5	1	1.25	0.10	1/2	106
3	5	40	1.25	0.05	1/4	13
4	5	40	1.25	0.10	1/2	106

5	200	40	1.25	0.10	1/12	6.5
6	300	40	1.25	0.10	1/16	6.3
7	215	28	1.25	0.10	1/14	6.5
8	200	20	1.25	0.10	1/12	7.4
9	225	20	1.25	0.10	1/14	6.5
10	250	20	1.25	0.10	1/16	6.5

(a). Mean flow with Isolated Roughness, Cases 1 and 2

First, the mean flow profiles obtained with single roughness, Cases 1 and 2, are presented. The roughness is located at $x_0 = 5$ mm, the width of the roughness is $w = 1.25$ mm and the roughness heights are $h = 0.05$ and 0.10 mm. The boundary layer thickness at $x = 5.0$ mm is about 0.20 mm. The heights of the roughness in terms of the boundary layer thickness are $h/\delta = 1/4$ and 1/2 respectively. The roughness Reynolds number, Re_{kk}, based on the flow variables at the roughness height and at $x = 5$ mm are 13 and 106 for the roughness heights $h/\delta = 1/4$ and 1/2 respectively. Figure 8(a) shows the density contours very close to the roughness. The figure shows the compression waves formed in front and back of the roughness element. The compression wave formed in front of the roughness is stronger than that at the trailing edge. The compression wave intersects the main shock and deflects the main shock slightly. The compression wave at the trailing edge is at a smaller angle and merges with the main shock further downstream. Figures 9(a) and (b) depict the streamline patterns over the roughness for the roughness heights $h = 0.05$ and 0.10 mm, respectively. At smaller roughness, the streamlines follow the roughness without significant separation. At the larger roughness case, $h = 0.10$ mm, the flow separates upstream and downstream of the roughness. The flow separates at $x = 4.6$ mm in the front of the roughness and attaches below the crest. The length of the separation bubble is about $4h$. The flow separates at the trailing edge of the crest and reattaches at $x = 6.35$ mm. The length of the bubble is about $1h$. Figure 10(a) shows the surface pressure distribution obtained with and without the roughness for the two roughness heights $h = 0.05$ and 0.10 mm. The figure clearly shows the strong pressure rise in front of the roughness, followed by an over expansion over the roughness and recompression near the trailing edge of the roughness. Figure 13 shows the variation of the amplitude of the pressure fluctuations along the wall computed using the non-parallel PSE method for the mean flows obtained with and without roughness. The stability calculations show that the isolated roughness height of $h/\delta = 1/4$ did not produce any noticeable difference in the stability of the boundary layer.

(b). Mean flow with Distributed Roughness, Cases 3-10

Since the effects of small isolated roughness on the stability of the boundary layer are weak, we concentrated on the effects of distributed roughness on the receptivity and stability of the boundary layer. As we discussed in the introduction and in the simulation results without roughness, the boundary layer is more receptive to external disturbances in three different regions, namely the nose region, the continuous spectrum and the synchronization point regions. Hence we spanned the roughness elements across these three regions and performed the simulations. We included in Fig. 1(a) the locations and the extents of different roughness patches we considered in the simulations. The parameters of the different roughness are given in Table 3. Patches 3 and 4 span across the nose region from $x_0 = 5$ mm to 105 mm, patch 5 spans across the continuous spectrum region from $x_0 = 200$ mm to 300 mm and patch 6 spans across the synchronization region from $x_0 = 300$ mm to 400 mm. The roughness parameters are $h = 0.05$, 0.10 mm, $w = 1.25$ mm, and $N = 40$. The distance between roughness elements is 2.5 mm. We found from the simulation results that the roughness patch 5 located across the continuous spectrum region causes the highest increase in the amplitudes of the instability waves. Hence to identify and understand which part of the continuous spectrum region is causing this increase the simulations were repeated, systematically decreasing the number of roughness and shifting the locations. Patch 7 spans across the continuous spectrum region from 215-285 mm with 28 roughness elements. In the Cases 8, 9 and 10 we placed 20 roughness elements at three locations 200-250, 225-275 and 250-300 mm, respectively.

Similar to the single roughness case, we first present the mean flow field produced by the distributed roughness for the Case 4. The distributed roughness spans from $x = 5$ mm to $x = 105$ mm and the roughness parameters are $h = 0.10$ mm, $w = 1.25$ mm, and $N = 40$. The distance between two roughnesses is 2.5 mm. Figs. 8(b), 9(c) and 10(b) display the density contours, streamlines over the roughness, and the pressure distributions along the distributed

roughness The results first show that as the boundary layer evolves over the roughness a pattern of compression, expansion, and another compression wave is formed over each element. However, the strength of these waves decreases with successive roughness. It is also observed that there exists a strong expansion and a compression at the end of the roughness $x \sim 105$ mm (Fig. 10(b)) before the pressure recovers back to the unperturbed pressure. Hence at the trailing edge there exists an adverse pressure gradient. This may in some cases make the flow separate downstream of the roughness. Similar to the single roughness case, the flow separates upstream and downstream of roughness. However, the upstream separation bubble becomes smaller for downstream roughness and by $x \sim 61.5$ mm (near the 25th roughness element), the flow does not separate ahead of the roughness. The downstream separation bubble becomes stronger. At the end of the distributed roughness the trailing-edge separation bubble length is about $3h$.

In Figs. 11 and 12 we compared the mean density profiles at different axial stations obtained with and without roughness. Figure 11 depicts the results for the Case 4 where $x_0 = 5$ mm, $h = 0.1$ mm, $N = 40$. Figures 11(a, b) show the density and velocity profiles immediately downstream of the roughness at $x = 110$ mm and further downstream at $x = 200$ mm. In Figure 11(c), we plotted the differences in the meanflow density profiles to discern the effects due to roughness clearly. The maximum differences occur near the edge of the boundary layers and immediately downstream of the roughness. The maximum difference in density is about twenty percent at $x = 110$ mm. The difference decays downstream and reaches about one percent near $x \sim 200$ mm. As evident from Figs 11(a, b), the boundary layer recovers to the smooth wall case by $x = 200$ mm. Similarly, Figures 12(a-c) show the density differences obtained with and without roughness for the Cases 9, 7 and 5, respectively. The maximum difference for the 20 roughness case is about six percent immediately downstream of the roughness and decays to about half a percent near $x \sim 350$ mm. The maximum differences are about ten percent for the 28 and 40 roughness cases. These differences decay to about one percent by $x \sim 350$ mm. The boundary layers fully recover to the unperturbed profiles within about 50 mm from the roughness.

Roughness influences the stability of the boundary layers in two ways. One is they interact with the free stream unsteady disturbances and modify the initial amplitude of the stability waves. The other is that they alter the boundary layer downstream and consequently they alter the stability characteristic of the boundary layer. Figure 13 shows the stability computations performed using the PSE method for the Cases 1, 3, and 4 where the roughness is located close to the nose region. The results show that the distributed roughness located near the nose region of the cone stabilized the downstream boundary layer. The maximum amplitudes decrease by factors of 1.2 and 1.4 times from the smooth cone case for the roughness heights of $h/\delta = 1/4$ and $1/2$ respectively.

(c). Interaction of Slow, Fast Acoustic Waves and Vorticity Waves with a Two-dimensional Isolated Roughness

After computing the mean flow, two-dimensional slow/fast acoustic disturbances $\tilde{p}_{ac}/p_\infty = 1*10^{-6}$ and vorticity disturbances $\tilde{u}/U_\infty = 1*10^{-6}$ at an incidence angle of 0 degrees were introduced at the outer boundary of the computational domain and time-accurate simulations were performed. The results are presented for a frequency of $F = 1.5*10^{-4}$ (217 kHz) and with $h = 0.05$mm, $w = 1.25$ mm, Case 1. Contours of the density fluctuations over the roughness generated by the interactions are shown in Figs. 14(a-c). The slow acoustic wave generates the unstable eigenmodes near the nose region. After that, the waves evolve downstream determined by the characteristics of the boundary layer. The figures show that well organized disturbances approach the roughness element from upstream and transmit through the compression waves unmodulated. The wavelength of the disturbances in this case is about 2.7 times longer than the width of the roughness. A parametric study increasing the width and height of the roughness is needed to see whether this conclusion remains the same. Figures 15(a-c) show the wall pressure fluctuations generated by the interactions for all three cases. Also included are the results obtained in the smooth case. It is seen that there are no differences in the amplitudes of the disturbances downstream of the roughness in all the cases. Hence for these parameters, $h/\delta = 1/4$, the roughness does not influence the receptivity of the disturbances generated by the free stream acoustic and vortical disturbances.

(d). Interaction of Slow, Fast Acoustic Waves and Vorticity Waves with Two-dimensional Distributed Roughness

Similar to the previous isolated roughness case, simulations are performed with multiple roughness elements. First let us discuss the results obtained for the Cases 3 and 4 where the roughness spans the nose region from $x = 5$ to 105 mm. The roughness parameters are $h = 0.05$ and 0.10 mm with $w = 1.25$ mm, $N = 40$. Figure 16 shows the contours of the density fluctuations generated by the interaction of the slow acoustic wave with the roughness elements. Notice that the perturbations are located at the edge of the boundary layer. Qualitatively, the picture conveys that roughness does not influence the structure of the disturbances. The structures evolve on top of the roughness elements without much deformation. Figures 17 and 18 give the quantitative comparison of the wall pressure fluctuations generated by the interaction of a slow acoustic wave with a smooth and a rough cone. Figure

17 depicts the results very close to the roughness and Fig. 18 depicts the results for the entire domain. Figures 17(a) and 18(a) show the results for the roughness height $h = 0.05$ mm and Figs. 17(b) and 18(b) show the results for the case $h = 0.10$ mm. Downstream of the roughness elements, $x \sim 105$ mm, the amplitudes of the disturbances are smaller for the cases with the roughness compared to that without the roughness. This reduction increases with the height of the roughness. The maximum pressure fluctuations amplitude ratios without and with the roughness are about 1.35 and 1.95 for the roughness heights $h = 0.05$ and 0.10 mm, respectively. Figure 13 showed that the amplitude reductions due to the stability part are 1.2 and 1.4 for these two roughnesses. Hence, receptivity of the instabilities, downstream of the roughness decreased by factors of 1.1 and 1.4 due to the distributed roughness heights $h = 0.05$ and 0.10 mm, respectively. This shows that a series of roughness elements reduces the receptivity coefficients of the instability waves generated by the free stream disturbances and also stabilizes the downstream boundary layer. However, these effects are too small to have an influence on the transition induced by the second modes. Figures 19(a-c) show the pressure fluctuations generated by the slow and fast acoustic waves and the vorticity waves along the surface with and without the distributed roughness. The maximum amplitudes obtained with the slow and fast acoustic waves and the vorticity wave are (0.021, 0.00021, 0.0076) without the roughness, and (0.015, 0.0002, 0.0071) with the roughness. This shows that the amplitudes of the second mode generated by the fast acoustic wave and the vorticity wave are not changed by the roughness.

Figure 20 depicts the results for the Case 6 where the roughness spans across the continuous spectrum, from $x = 200$ to 300 mm. The figure shows the variation of the maximum wall pressure fluctuations along the wall. The maximum amplitudes obtained with roughness for this case are (0.098, 0.001, 0.08). This shows that the roughness located across the continuous spectrum increased the receptivity by 4.6, 4.5 and 11.4 times compared to that without the roughness for the slow, fast acoustic disturbances, and the vortical disturbance, respectively. We also plotted the amplitude variation obtained from the PSE calculations performed on the meanflow without the roughness. It is interesting to note that downstream of the roughness $x > 300$ mm, the PSE computations obtained without the roughness agree very well with those obtained with roughness in all three cases. This suggests that the stability characteristics downstream of the roughness are not influenced or modified by the roughness. Only the initial amplitudes of the instability waves, i.e. the receptivity, downstream of the roughness are increased by the roughness. This increase is the highest for the vorticity waves by a factor of 2.5 compared to those for the slow and the fast acoustic waves.

Similarly, Fig. 21 shows the results for the Case 7 where the roughness is distributed across the synchronization point, $x = 300$ to 400 mm. The maximum amplitudes obtained with roughness for this case are (0.022, 0.00025, 0.017). The amplitudes of the disturbances generated by the acoustic disturbances did not change in this case. However, the amplitude of the second mode generated by the vorticity wave increased by about 2.2 times compared to the smooth-wall case. This increase is smaller by a factor of five compared to the previous case where the roughness was located across the continuous spectrum. Thus, the roughness elements located across the continuous spectrum or upstream of the synchronization point are more effective in increasing the amplitude of the instability waves compared to roughness elements located outside of this region.

As we discussed previously, to identify and understand which part of the continuous spectrum region is causing this increase we performed the simulations with roughness patches decreasing in sizes and locations. We performed several simulations and will present the results for the Cases 8-11. The roughness patches in these cases 8, 9, 10 and 11 span across 215-285, 200-250, 225-275 and 250-300 mm, respectively. The number of roughness is also correspondingly decreased from 28 to 20. In the last three cases, we fixed the number of roughness to 20 and shifted the locations of the roughness patch to 200, 225 and 250 mm, respectively. The different arrangements of the roughness with respect to the stability characteristics of the boundary layer are illustrated in Fig. 1(a). Figure 22 shows the variation of the maximum wall pressure fluctuations generated by the interaction of vorticity waves with different roughness distributions. We also include the results obtained for the Case 5, where 40 roughness elements were placed across $x = 200$ to 300 mm. It is also noted that the PSE calculations performed for the meanflow obtained without the roughness agrees very well with the results obtained with roughness for all the cases. This suggests that the meanflow recovers back to the smooth case meanflow in a short distance downstream. The maximum amplitudes obtained for the Cases 8-11 are (0.054, 0.03, 0.016, .07). The maximum amplitude obtained without the roughness is 0.007. The ratios of the maximum amplitudes obtained with roughness compared to the smooth wall case are (7.7, 4.3, 2.3, 10.0), respectively. The important observation is that the roughness patch that spans from 250-300 mm with 20 roughness elements (Case 11) generated almost the same amplitude curve as that generated by the long roughness patch that spans from 200-300 mm with 40 roughness elements (Case 6). This region consists of the continuous spectrum region and the neutral point for the second mode instability wave. Hence this region 250-300 mm that contains the continuous spectrum and the neutral point appears to be the most sensitive region for the roughness to have the strongest influence on the receptivity of the boundary layer to free stream disturbances. The simulation results conclude that the roughness generates the instability wave with larger amplitude

further upstream compared to the smooth wall case. One interesting observation is that the maximum amplitude curve reaches a minimum value before the disturbances started to grow due to instability. For example, for the 40 roughness case the amplitude reaches a minimum value at $x = 285$ mm. With decreasing length of the roughness patch, this minimum point moves downstream. At this point we do not know the significance of this observation and it needs further investigation.

2. Three-dimensional Roughness Cases

Similar to the two-dimensional roughness cases, simulations are performed with one row of three-dimensional roughness elements with rectangular planforms (Figs. 2d, 2e). The shape of the roughness is given by eq. (2). The roughness elements are placed periodically in the azimuthal direction with the wavenumber *m*. Hence the wavelength between the roughness is $2\pi/m$. In the simulations, the width of the roughness in the azimuthal direction is taken as half of the wavelength π/m. The simulations are performed for a roughness located at $x_0 = 25$ mm. The roughness heights are $h = 0.05$ and 0.10 mm, the roughness length is $w = 1.25$ mm, and the azimuthal wavenumber of the roughness is $m = 16$. The boundary layer thickness at $x = 25$ mm is about 0.5 mm. The heights of the roughness in terms of the boundary layer thickness are $h/\delta = 1/8$ and $1/4$ respectively. The roughness Reynolds number, Re_{kk}, based on the flow variables at the roughness height and at $x = 25$ mm are 10 and 22 for the roughness heights $h/\delta = 1/8$ and $1/4$ respectively.

(a). Mean Flow with Three-dimensional Roughness Elements – Single Row

Figure 23(a-c) shows the density contours and the streamlines in the symmetry plane, $\theta = 0$, over the roughness. The figure shows the compression wave formed in front of the roughness element, an over expansion over the roughness, and the final recompression downstream to recover with the pressure distribution over the smooth cone. Figures 23(b) and (c) show that the flow separates upstream and downstream of the roughness. However, the separation bubble in this case is three-dimensional. The lengths of the separation regions along the symmetry plane are about $2h$ in upstream and downstream directions. Figure 24 depicts the azimuthal velocity contours in several cross-sectional planes over the roughness and downstream of the roughness. It is noted that the azimuthal velocities induced by the roughness is small, on the order of one percent of the freestream velocity. The perturbations almost decayed to zero by $x \sim 30$ mm. Figures 25(a-c) show the streamline patterns over the roughness. Figure 25(a) shows the streamlines originating from the grid line $J = 2$ or $y_n = 0.01$ mm and Figs, 25(b) and (c) show the streamlines originating at $y_n = 0.02$ and 0.10 mm respectively. It is interesting to see that streamlines very close to the surface are completely diverted sideways by the roughness. The streamlines approaching the roughness at the same height as the roughness flows over the roughness without much modulation.

(b). Interaction of Slow Acoustic Waves with Three-dimensional Roughness – Single Row

After the steady mean flow with the roughness is computed, unsteady slow acoustic disturbances are superimposed at the outer boundary of the computational domain and time accurate simulations are performed. The amplitude of the slow acoustic disturbances is $\tilde{p}_{ac} / p_\infty = 1*10^{-5}$ and the frequency of the disturbances is $F = 1.5*10^{-4}$ (217 kHz). Figure 26 shows the contours of the density fluctuations along the symmetry plane, $\theta = 0$, over the roughness with a height of $h = 0.05$ mm. It is seen that the incoming two-dimensional boundary layer disturbances are propagating over the roughness and across the shock waves generated by the roughness without any noticeable modification. Figures 27(a) and (b) depict the contours of the density and the azimuthal velocity disturbances generated by the interaction of the roughness and the two-dimensional slow acoustic wave in the plan view, $(x$-$r\theta)$ plane, across the middle of the boundary layer. The figure shows that the density fluctuations remain two-dimensional downstream of the roughness. This illustrates that at small roughness heights, the incoming two-dimensional disturbances are not influenced by the roughness. However three-dimensional roughness, due to the interaction with the two-dimensional acoustic disturbances generates additional three-dimensional instability waves downstream of the roughness. This is clearly observed in Fig. 27(b). The figure shows the generation and the growth of the azimuthal disturbances downstream of the roughness.

Figures 28(a) and (b) show the quantitative results of the disturbances generated by the interaction of the roughness and the slow acoustic wave. Figure 28(a) depicts the wall pressure fluctuations along the wall in the symmetry plane and Fig. 28(b) shows the azimuthal velocity fluctuations in the middle of the boundary layer. In Fig. 28(a), we also included the wall pressure fluctuations obtained without the roughness. It is seen that the two-dimensional disturbances are not modified by the isolated roughness. Figure 28(b) shows the generation and the growth of a three-dimensional disturbance. To investigate how the disturbances are evolving, a Fourier analysis is performed in the azimuthal direction. The disturbances are decomposed into the following form.

$$p(x,r,\theta,t) = \left\{ \sum_{m=-M}^{M} \tilde{p}_m(x,r)e^{im\theta} \right\} e^{-i\omega t} + c.c,$$

Figure 29(a) shows the amplitude of the Fourier component $\left| \tilde{p}_m(x,r) \right|$ as a function of the azimuthal wavenumber m for the pressure distribution on the surface of the cone at different axial locations $x =$3.362, 6.562 and 10.162 cm. The spectrum as expected has the largest value for the two-dimensional disturbance m=0 and it then decreases to very small values. The spectral amplitudes for m=0 and 16 at x=3.362 cm are $2.3*10^{-5}$ and $3.9*10^{-8}$, respectively. This shows that the amplitude of the three-dimensional wave generated by the roughness of height h=0.05 mm is about 590 times smaller than the two-dimensional disturbance. Figure 29(b) depicts the evolution of the amplitudes of the modes m = 0 and 16. As we observed in the two-dimensional distributed roughness simulations, the distributed three- dimensional roughness may increase the amplitude of the three-dimensional wave by orders of magnitude, however those simulations are beyond the scope of the present investigation.

VI.   Conclusions

The effects of two-dimensional distributed roughness elements located in the nose region, across the continuous spectrum, and across the synchronization point on the receptivity and stability of the boundary layer were numerically investigated. The interaction of slow, fast, and vortical disturbances with the smooth and the rough cone were simulated. The interaction of a single row of three dimensional roughness elements of rectangular plan form was also investigated. Both the steady and unsteady solutions were obtained by solving the compressible Navier-Stokes equations using the 5th-order accurate weighted essentially non-oscillatory (WENO) scheme for space discretization and using a third-order total-variation-diminishing (TVD) Runge-Kutta scheme for time integration.

The two-dimensional distributed roughness elements located near the nose region produced a small decrease in the receptivity coefficient of the instability waves generated by the slow acoustic wave. The results also showed that the boundary layer downstream of the roughness becomes more stable compared to the smooth cone case. However, these effects are small. The distributed roughness elements located across the continuous spectrum increased the receptivity of the second mode generated by the slow and fast acoustic waves and the vorticity wave by about 4.6, 4.5 and 11.8 times, respectively. In this case, the amplitude of the second mode generated by the vorticity waves is almost the same as that generated by the slow acoustic mode. The distributed roughness elements located across the synchronization point increased the receptivity of the second mode generated by the vorticity wave by about 2.2 times and did not change the receptivity of the second mode generated by the slow and fast acoustic waves. The sensitivity to the location of the distributed roughness elements was systematically studied by shifting the location of the roughness elements. The roughness patch of half the size located in the continuous spectrum region yielded the same increase in receptivity compared to the longer patch of roughness.. At this point, we could not discern the effects of the continuous spectrum neutral point and the synchronization region separately. The results also revealed that the boundary layers downstream of the roughness recover to the smooth wall case in a short distance and the stability characteristics downstream of the roughness remain the same as the smooth wall case.

Simulations of the interaction of two-dimensional slow acoustic disturbances with a single row of three-dimensional roughness elements showed that small roughness elements do not enhance or suppress the incoming two-dimensional instability waves. However, due to the interaction, a three-dimensional wave is generated downstream of the roughness. The amplitude of the wave is about 590 times smaller than the amplitude of the two-dimensional instability wave for the case that was investigated. This conclusion might change for an interaction of acoustic wave with distributed roughness elements.

References

[1]Mack, L., "Boundary Layer Stability Theory," JPL Report No. 900-277 Rev. A, Pasadena, Calif, Nov. 1969.

[2]Kendall,J. M., "Wind Tunnel Experiments Relating to Supersonic and Hypersonic Boundary-Layer Transition ," *AIAA J.,* Vol. 13, No. 3, 1975, pp. 290-299.

[3]Stetson, K. F., Thompson, E. R., Donaldson, J. C., and Siler, L. G., "Laminar Boundary Layer Stability Experiments on a Cone at Mach 8, Part 1: Sharp Cone," AIAA 22nd Aerospace Sciences Meeting, Reno, Nevada, January 9-12, *AIAA Paper 83-1761*, 1983.

[4]Stetson, K. F., and Kimmel, R. L., "On Hypersonic Boundary-Layer Stability," AIAA Paper 92-0737, January 1992.

[5]Blanchard, A.E., "An Investigation of Wall-Cooling Effects on Hypersonic Boundary-Layer Stability in a Quiet Wind Tunnel", Ph.D. Dissertation, Old Dominion University, Dept. of Mechanical Engineering, Norfolk, VA, December, 1995.

[6]Lachowicz, J, T., Chokani, N., and Wilkinson, S.P., "Boundary-Layer Stability Measurements in a Hypersonic Quiet Tunnel", *AIAA Journal*, Vol. 34, No. 12, December 1996.

[7]Wilkinson, S. P., "A Review of Hypersonic Boundary Layer Stability Experiments in a Quiet Mach 6 Wind Tunnel", AIAA Paper 97-1819, June 1997.

[8]Maslov, A. A., Shiplyuk, A. N., Sidorenko, A. A and Arnal, D., "Leading Edge Receptivity of a Hypersonic Boundary layer on a Flat Plate," *J. Fluid Mech.,* Vol. 426, 2001, pp. 73-94.

[9]Wheaton, B., Juliano, T.J., Berridge, D.C., Chou, A., Gilbert, P.L., Casper, K.M., Steen, L.E., Schneider, S., and Johnson, H.B., "Instability and Transition Measurements in the Mach 6 Quiet Tunnel," AIAA Paper 2009-3559, June 2009.

[10]Casper, K.M., Beresh, S.J., Henfling, J.F., Spillers, R.W., Pruett, B., and Schneider, S.P., "Hypersonic Wind-Tunnel Measurements of Boundary-Layer Pressure Fluctuations," AIAA Paper 2009-4054, Jun 2009.

[11]Malik, M. R., "Boundary-Layer Transition Prediction Toolkit," AIAA Paper 1997-1904.

[12]Gushin, V. R., and Fedorov, A. V., "Excitation and development of unstable disturbances in supersonic boundary layer," *Fluid Dynamics*, Vol. 25, No. 3, 1990, pp. 344-352.

[13]Fedorov, A. V., and Khokhlov, A. P., "Prehistory of Instability in a Hypersonic Boundary Layer," *Theoret. Comput. Fluid Dynamics*, Vol. 14, pp. 359-375, 2001.

[14]Fedorov, A. V., and Khokhlov, A. P., " Excitation of Unstable Modes in a Supersonic Boundary Layer by Acoustic Waves," *Fluid Dynamics*, Vol. 26, No. 4, pp. 531-537, July 1991.

[15]Fedorov, A. V., and Khokhlov, A. P., "Sensitivity of a Supersonic Boundary Layer to Acoustic Disturbances," *Fluid Dynamics*, No. 27, pp. 29-34, 1992

[16]Fedorov, A.V., "Receptivity of a High-Speed Boundary Layer to Acoustic Disturbances," *J. Fluid Mech.*, Vol. 491, 2003, pp. 101-129.

[17]Fedorov, A.V., "Transition and Stability of High-Speed Boundary Layers," *Annu. Rev. Fluid Mechanics*, 2011. 43:79-95.

[18]Ma, Y. and Zhong, X., "Receptivity of a Supersonic Boundary Layer over a Flat Plate. Part 1. Wave Structures and Interactions," *J. Fluid Mech.*, Vol. 488, 2003, pp. 31-78.

[19]Ma, Y. and Zhong, X., "Receptivity of a Supersonic Boundary Layer over a Flat Plate. Part 2. Receptivity to Freestream Sound," *J. Fluid Mech.*, Vol. 488, 2003, pp. 79-121.

[20]Malik, M. R., and Balakumar, P., " Acoustic receptivity of Mach 4.5 boundary layer with leading edge bluntness,"*Theoret. Comput. Fluid Dynamics* . Vol. 21, pp. 323-342, 2007.

[21]Kara, K., Balakumar, P., and Kandil, O.A., "Receptivity of Hypersonic Boundary Layers Due to Acoustic Disturbances over Blunt Cone," AIAA Paper 2007-945, Jan. 2007.

[22]Kara, K., Balakumar, P., and Kandil, O.A., "Effects of Nose Bluntness on Stability of Hypersonic Boundary Layers over a Blunt Cone," AIAA Paper 2007-4492, June 2007.

[23]Kara, K., Balakumar, P., and Kandil, O.A., "Effects of Wall Cooling on Hypersonic Boundary Layer Receptivity over a Cone," AIAA Paper 2008-3734, June 2008.

[24]Kara, K. Balakumar, P. and Kandil, O. A., "Effects of Nose Bluntness on Hypersonic Boundary Layer Receptivity and Stabilityover Cones," *AIAA Journal*, Vol. 49, No. 12, December 2011, pp. 2593-2606.

[25]Balakumar, P., and Kegerise, M. A., "Receptivity of Hypersonic Boundary Layers over Straight and Flared Cones," AIAA Paper 2010-1545, January 2010.

[26]Balakumar, P., and Kegerise, M. A., "Receptivity of Hypersonic Boundary Layers to Acoustic and Vortical Disturbances," AIAA Paper 2011-0371, January 2011.

[27]Reda, D. C., "Review and Synthesis of Roughness-Dominated Transition Correlations for Reentry Applications," *J. Spacecraft and Rockets,* 39 2:161-167.

[28]Schneider, S. P., "Summary of Hypersonic Boundary-Layer Transition Experiments on Blunt Bodies with Roughness," *J. Spacecraft and Rockets,* 45 6:1090-1105.

[29]Holloway, P., and Sterett, J., "Effect of Controlled Surface Roughness on Boundary-Layer Transition and Heat Transfer at Mach Numbers of 4.8 and 6.0," NASA, TR TN D-2054, 1964.

[30]Fujii, K. "Experiment of the Two-Dimensional Roughness effect on Hypersonic Boundary-Layer Transition," *J. Spacecraft and Rockets*, Vol.43, No. 4, July-August 2006.

[31]Marxen, O., Iaccarino, G., and Shaqfeh, E. S., "Disturbance Evolution in a Mach 4.8 Boundary Layer with Two-Dimensional Roughness-Induced Separation and Shock," *J. Fluid Mech*. (2010). Vol. 648, pp. 435-469.

[32]Bountin, D., Chimitov, T., Maslov, A., Novikov, A., Egorov. I, and Fedorov, A., "Stabilization of a Hypersonic Boundary Layer using a Wavy Surface," AIAA-2012-1105, January 2012.

[33]Balakumar, P., "Receptivity of Hypersonic Boundary Layers to Distributed Roughness and Acoustic Disturbances," AVT-Specialists' Meeting on Hypersonic Laminar-Turbulent Transition, April 16-19, 2012, San Diego, CA.

[34]Shu, C.W., Essentially Non-Oscillatory And Weighted Essentially Non-Oscillatory Schemes For Hyperbolic Conservation Laws, NASA/CR-97-206253 and ICASE Report No. 97-6.

[35]Atkins, H.L., "High-Order ENO Methods for the Unsteady Compressible Navier-Stokes Equations," AIAA Paper 91-1557, 1991.

[36]Balakumar, P., Zhao, H., and Atkins, H., "Stability of Hypersonic Boundary Layers Over a Compression Corner," AIAA Paper 2002-2848, June 2002.
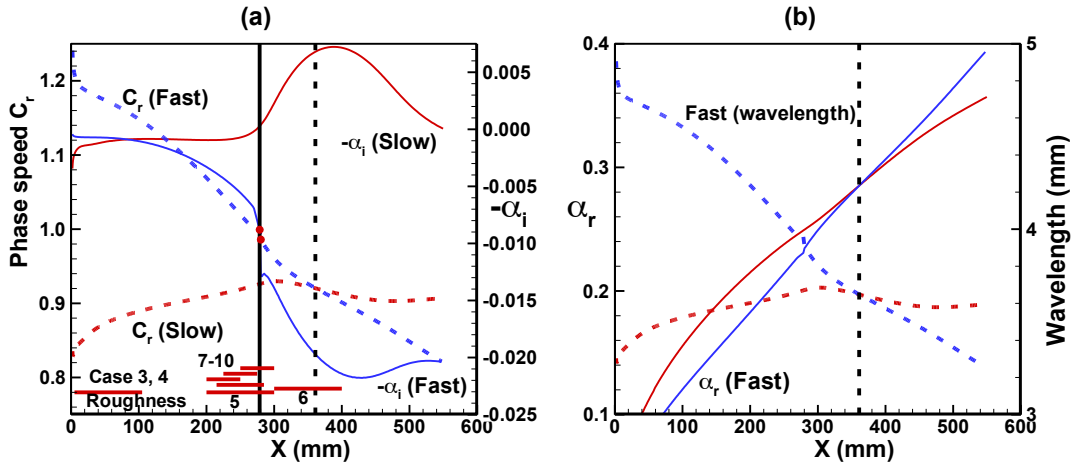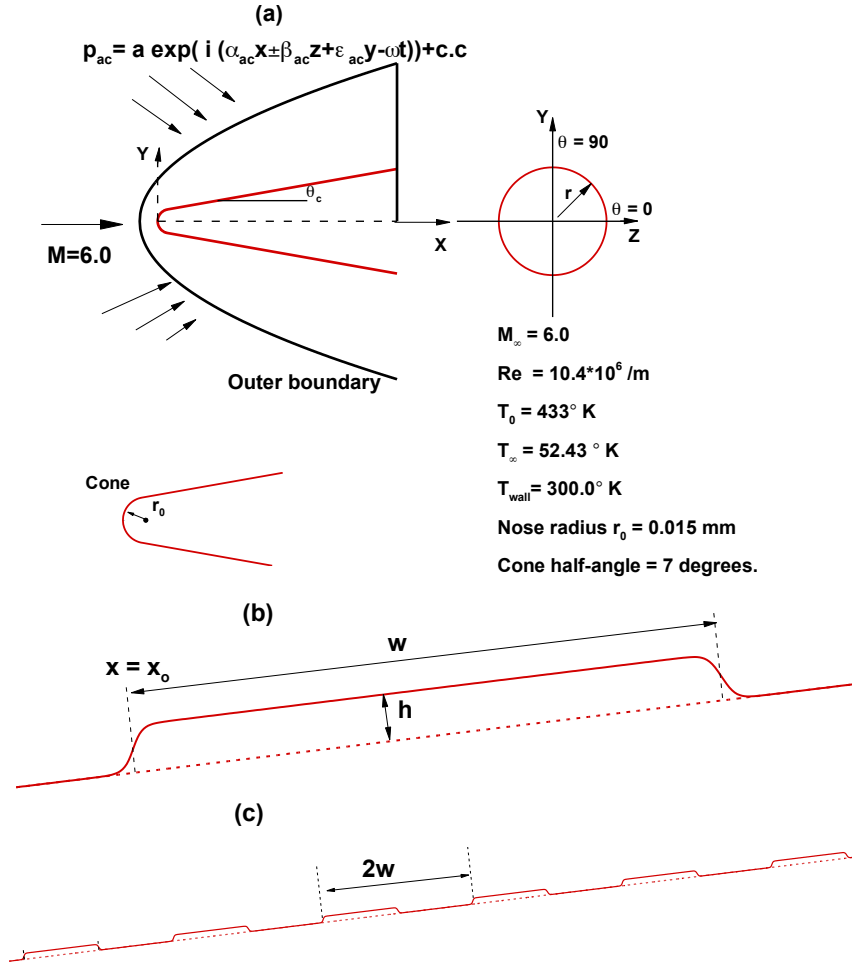
(a)

(b)

Figure 1. Eigenvalues from the linear stability computations for fast (blue) and slow (red) modes for a flow over an axi-symmetric cone at a free stream Mach number of M=6. The frequency is $F=1.5*10^{-4}$. (a) Phase speed c_r and growth rates $-\alpha_i$ and (b) wavenumber α_r and wavelength.
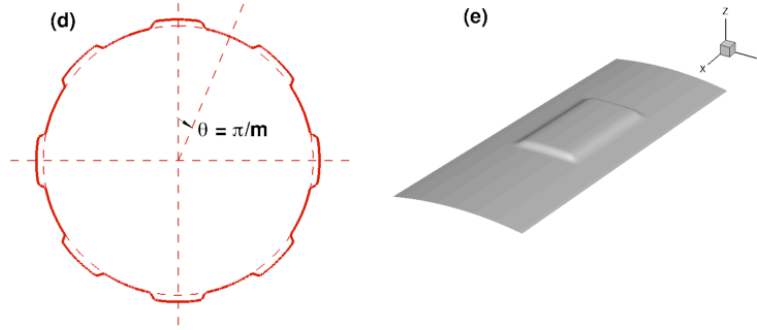
(a)

$p_{ac} = a \exp(i (\alpha_{ac}x \pm \beta_{ac}z + \varepsilon_{ac}y - \omega t)) + c.c$

$\theta = 90$

$\theta = 0$

M=6.0

Outer boundary

Cone

r_0

$M_\infty = 6.0$

$Re = 10.4*10^6$ /m

$T_0 = 433°$ K

$T_\infty = 52.43°$ K

$T_{wall} = 300.0°$ K

Nose radius $r_0 = 0.015$ mm

Cone half-angle = 7 degrees.

(b)

x = x_o

w

h

(c)

2w

American Institute of Aeronautics and Astronautics

Figure 2. Schematic diagrams of the (a) 7-degree sharp-tipped cone model and flow conditions, (b) a single roughness element, (c) the distributed roughness elements, (d) roughness distribution in the azimuthal direction, and (e) three-dimensional view of the roughness.
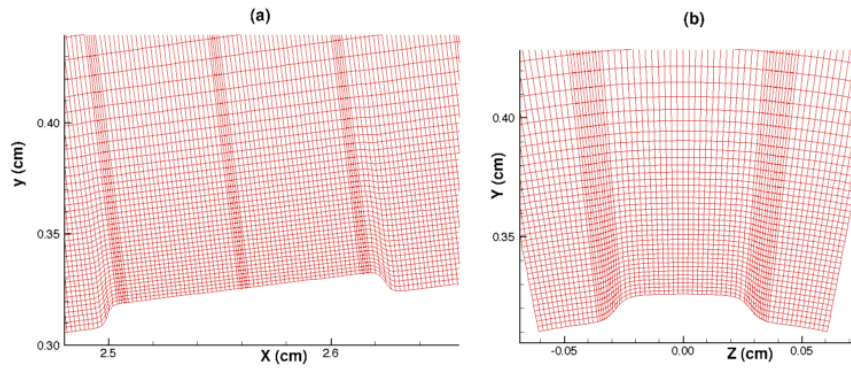
Figure 3. Grid distributions over one roughness element (a) in the axial (x-y) plane, and (b) in the azimuthal (y-z) plane.
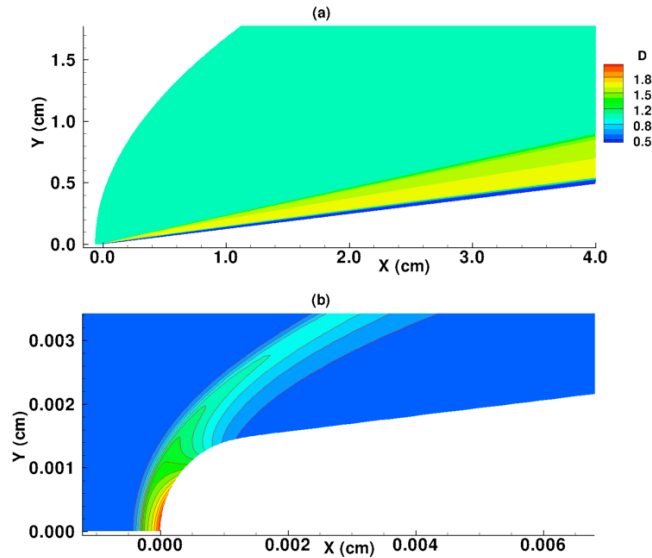
Figure 4. Mean density contours for flow over a 7-degree sharp-tipped smooth-wall cone at Mach 6.
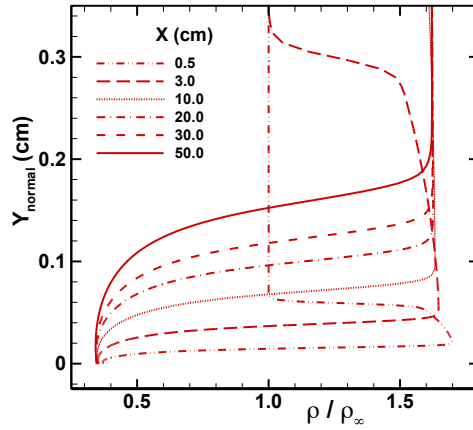
Figure 5. Boundary layer density profiles at different axial locations without roughness.
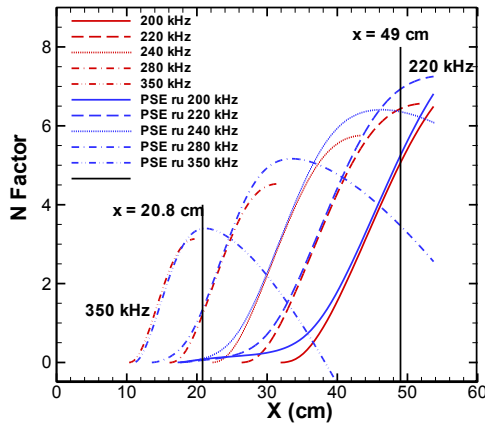
Figure 6. N-Factor curves computed from the linear stability analysis and the PSE analysis based on $(\rho u)_{max}$.
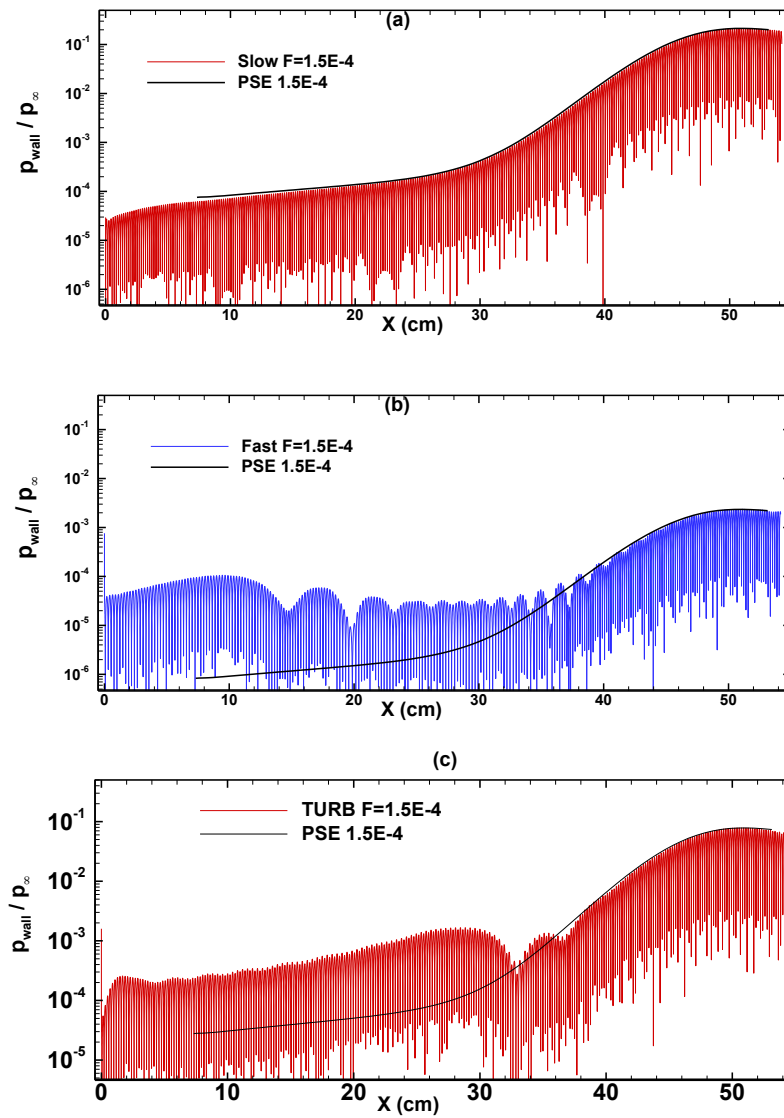
Figure 7. Wall pressure fluctuations generated by the interaction of (a) a two-dimensional slow acoustic wave (b) a fast acoustic wave and (c) an axi-symmetric vortical disturbances without roughness in log-scale for $F=1.5*10^{-4}$.
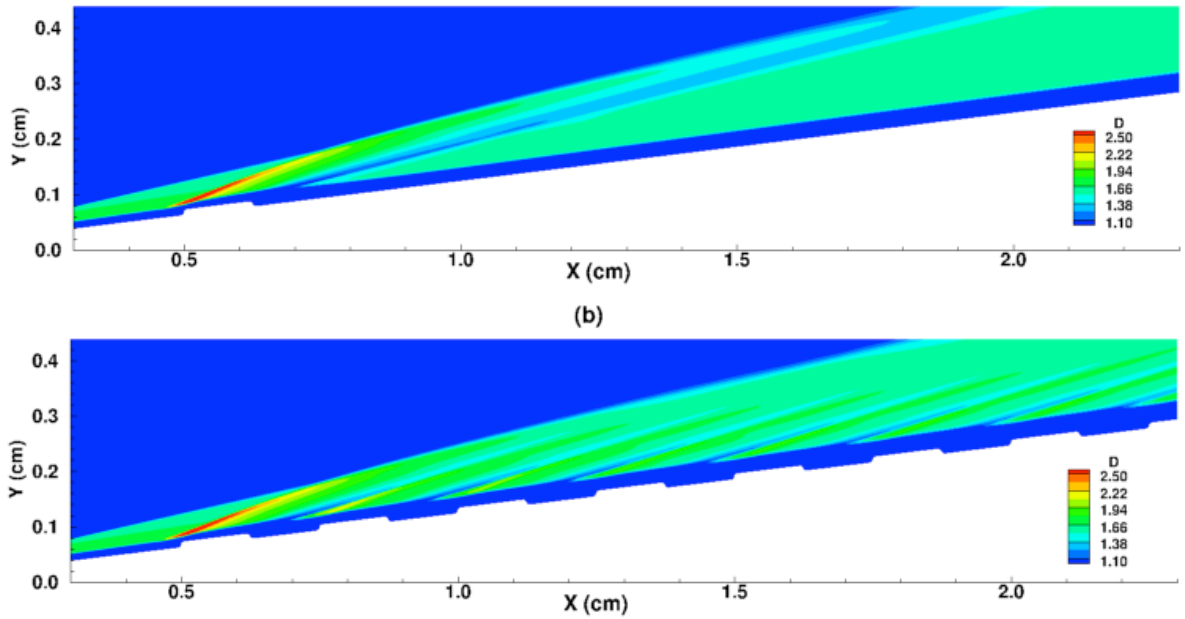
Figure 8. Mean density contours with (a) an isolated roughness, (b) distributed roughness for h=0.10 mm, w=1.25 mm, x_0=5mm.
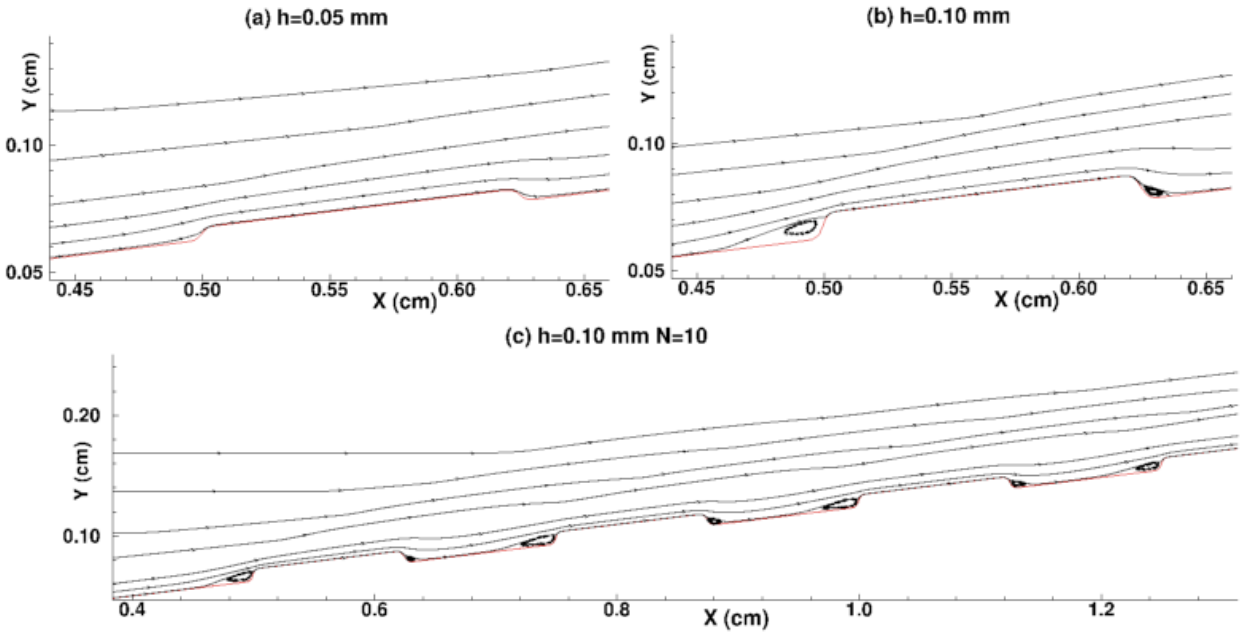
Figure 9. Streamline patterns for the flow over an isolated roughness (a) h = 0.05 mm (b) 0.10 mm, and (c) distributed roughness h = 0.10 mm, N=40. w = 1.25 mm, x_o = 5 mm.
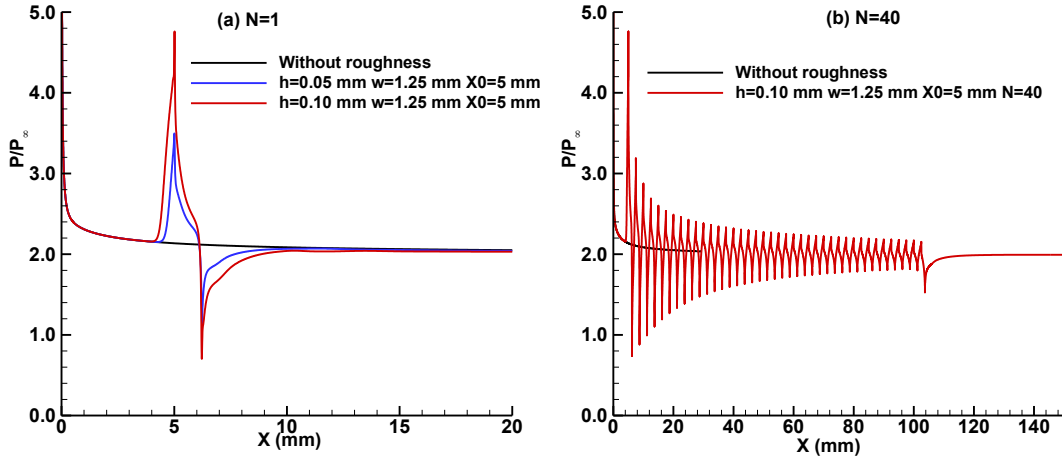
Figure 10. Surface pressure variation with and without roughness. (a) Isolated roughness (b) distributed roughness.
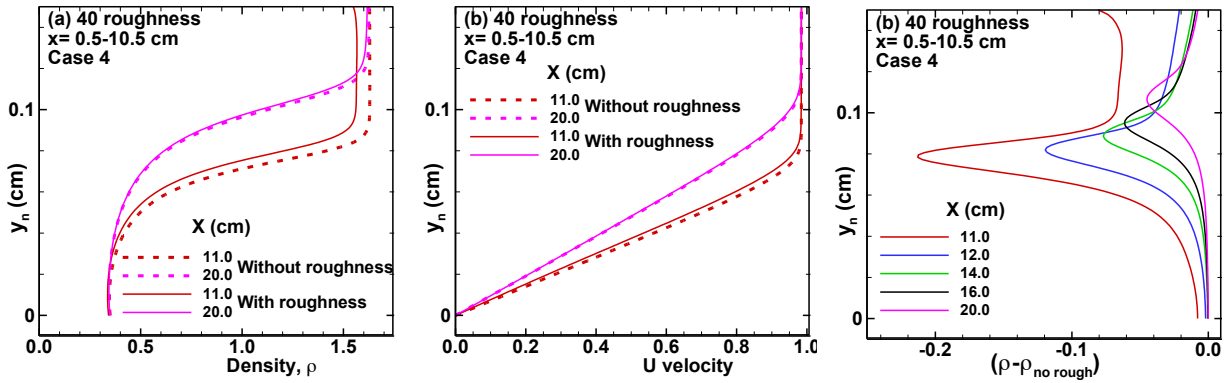
Figure 11. The mean density profiles obtained with and without distributed roughness for the Case 2, $x_0=200$ mm, h = 0.10 mm, N=40. (a) density profiles, (b) U velocity profiles, (c) density difference profiles.
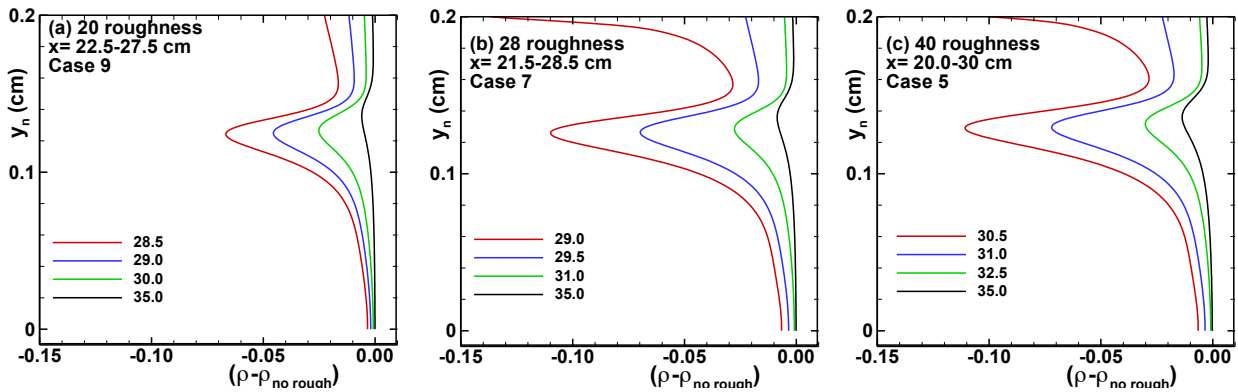
Figure 12. The differences in the mean density profiles between the profiles obtained with and without distributed roughness for the Cases 9, 7, 5: (a) $x_0=200$ mm, N=40, (b) $x_0=215$ mm, N=28, and (c) $x_0=225$ mm, N=20. h=0.10 mm w=1.25 mm, $F=1.5*10^{-4}$.
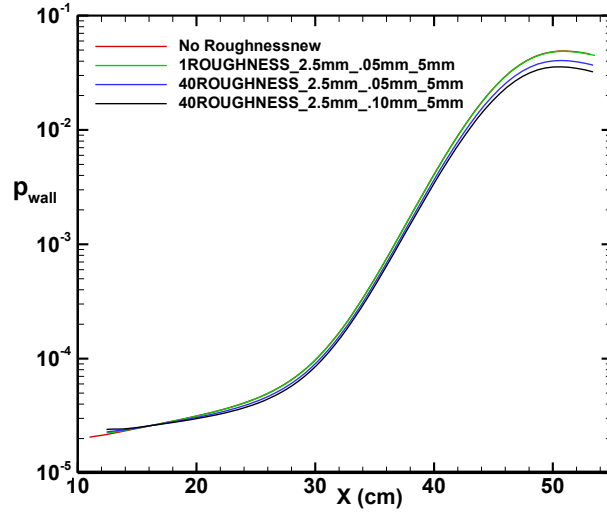
Figure 13. Variation of the amplitude of the pressure variation along the wall computed from linear PSE for different cases.
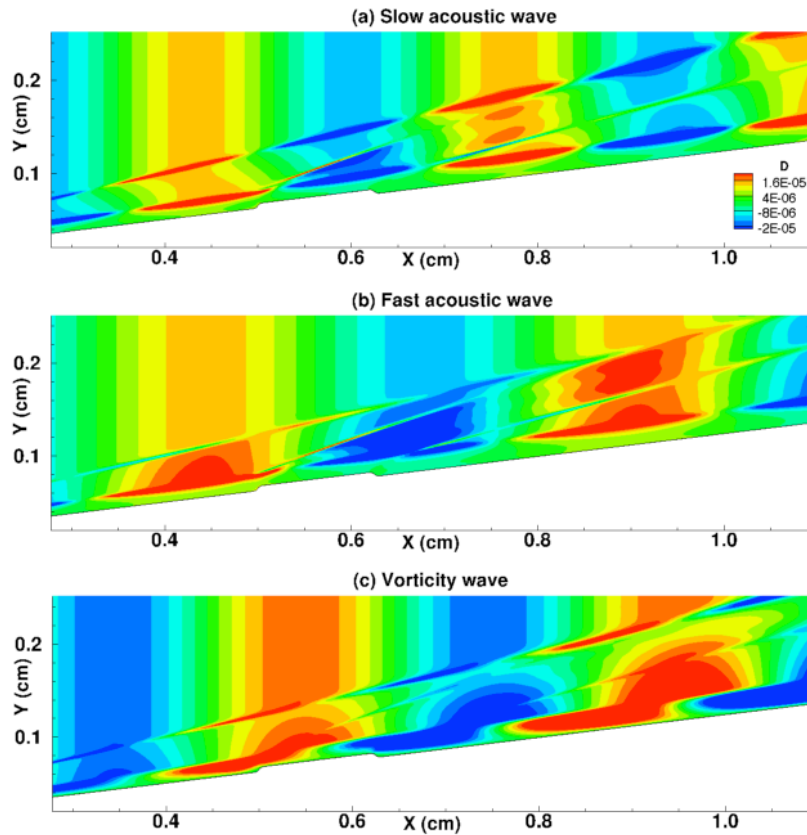
Figure 14. Density fluctuations generated by the interaction of (a) slow, (b) fast acoustic waves and (c) vorticity waves with an isolated roughness for *h=0.05 mm, w=1.25 mm, N=1, F=1.5*10⁻⁴*.
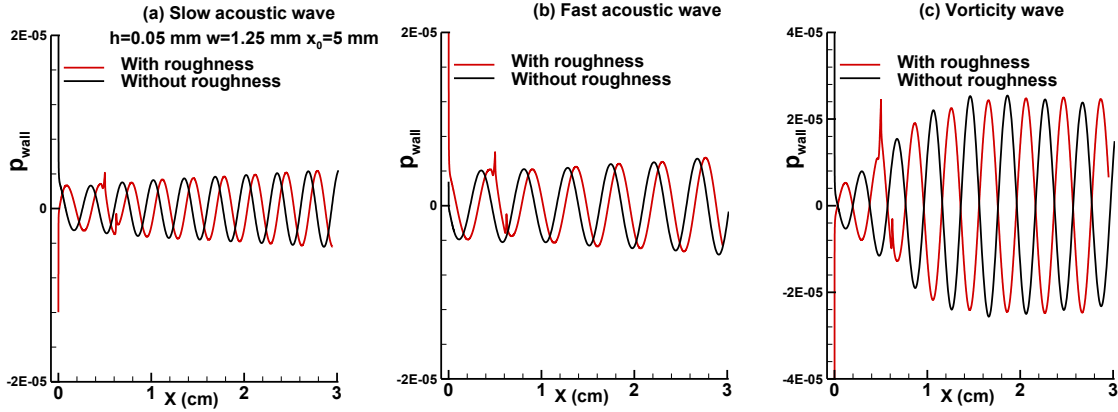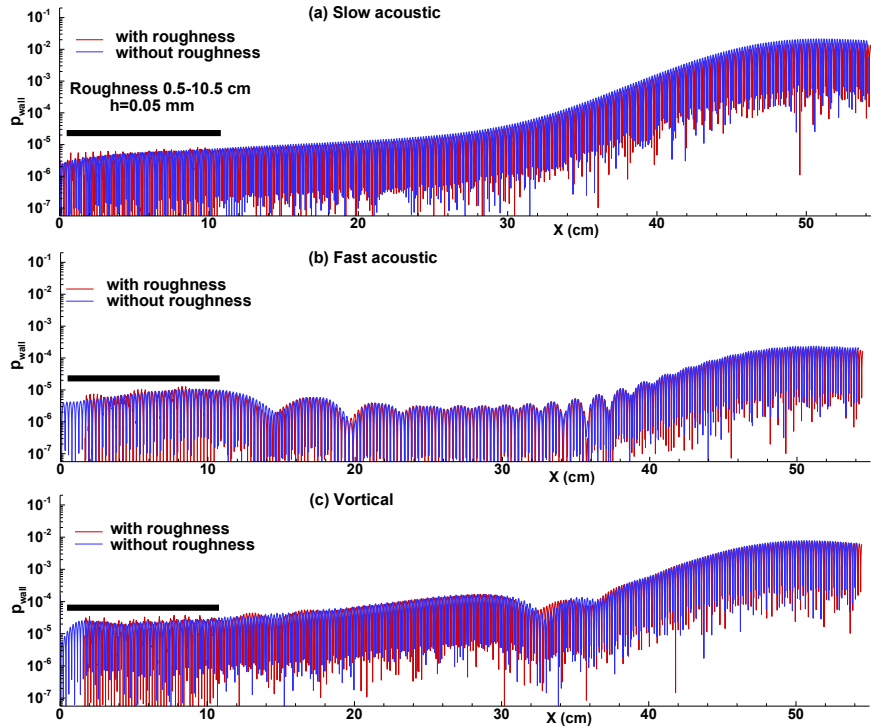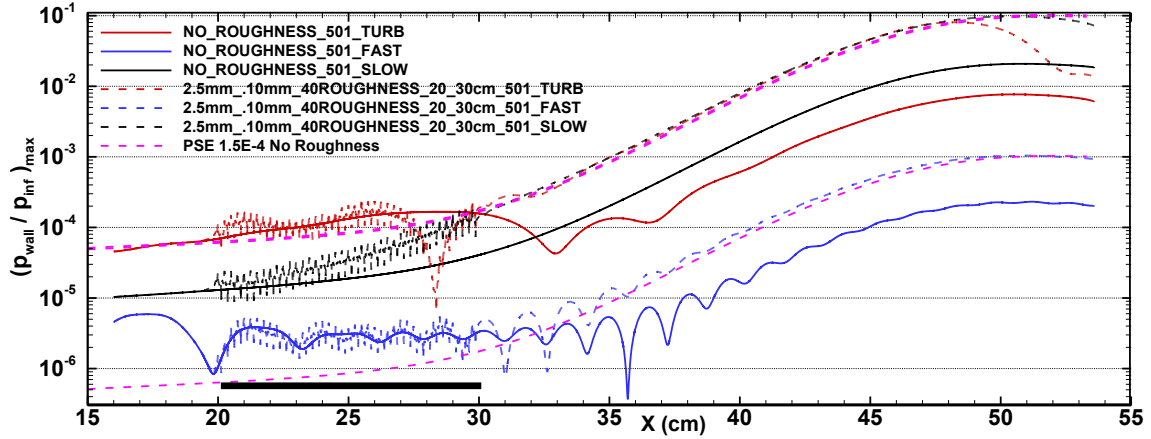
Figure 15. Wall pressure fluctuations generated by the interaction of (a) slow (b) fast acoustic waves and (c) vorticity waves with and without roughness for *h=0.05 mm, w=1.25 mm, N=1, F=1.5*10^{-4}*.
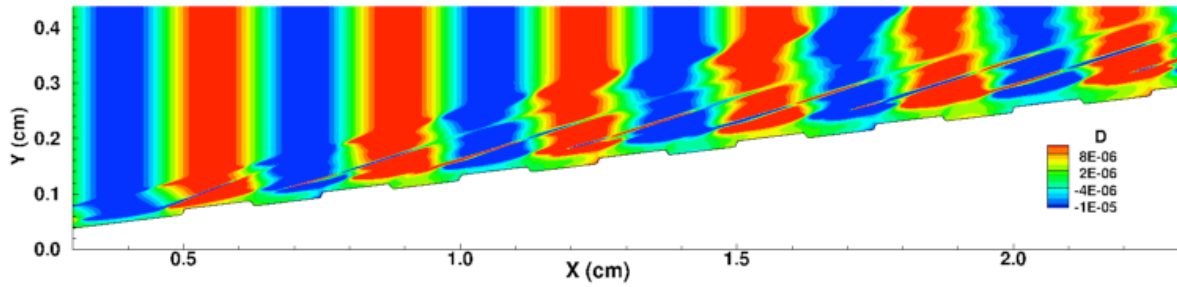
Figure 16. Density fluctuations generated by the interaction of a slow acoustic wave with distributed roughness for *x_0=5mm, h=0.10 mm, w=1.25 mm, N=40, F=1.5*10^{-4}*.
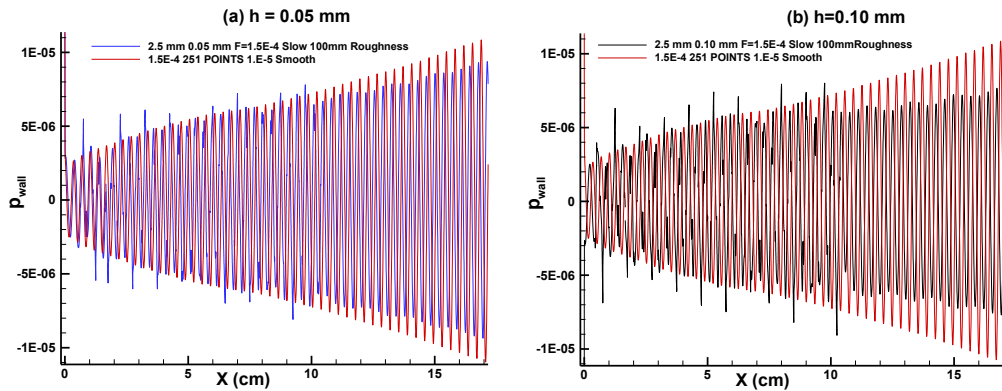
Figure 17. Wall pressure fluctuations generated by the interaction of a slow acoustic wave with distributed roughness. Close to the roughness. *(a) h=0.05 mm (b) h=0.10 mm. x_0=5mm, w=1.25 mm, N=40, F=1.5*10^{-4}*.
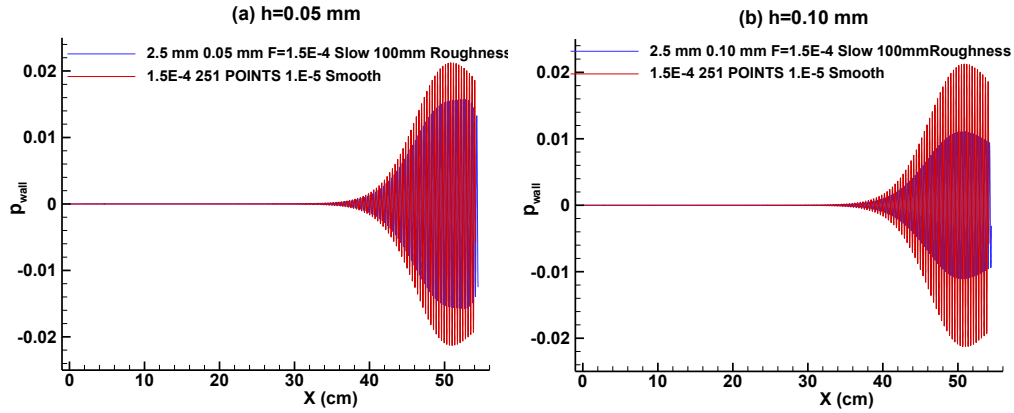
(a) h=0.05 mm

(b) h=0.10 mm

Figure 18. Wall pressure fluctuations generated by the interaction of a slow acoustic wave with distributed roughness. Further downstream. *(a) h=0.05 mm (b) h=0.10 mm. x_0=5mm, w=1.25 mm, N=40, F=1.5*10^{-4}.*
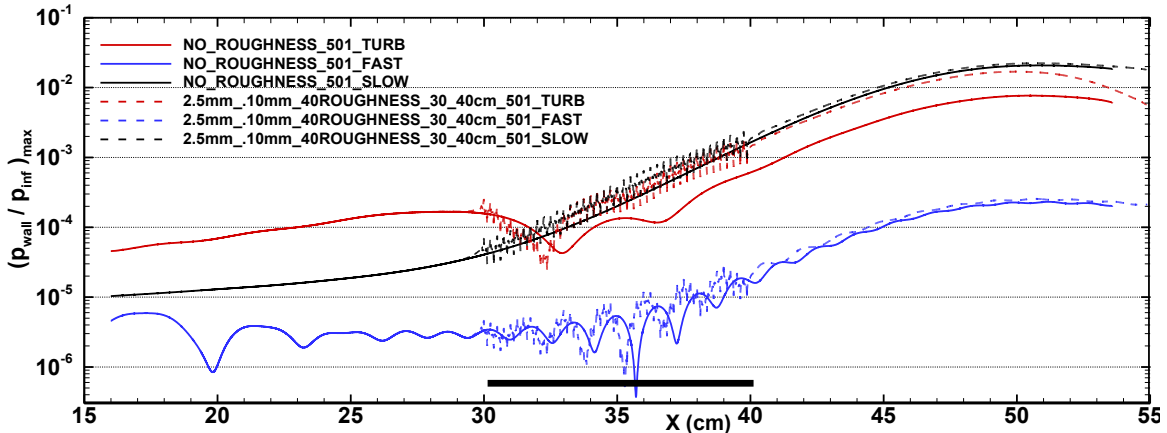
Figure 19. Wall pressure fluctuations generated by the interaction of (a) a slow acoustic wave (b) a fast acoustic wave, and (c) a vorticity wave with distributed roughness for the Case 1. *x_0=5mm, h=0.05 mm w=1.25 mm, N=40, F=1.5*10^{-4}.*

Figure 20. Wall pressure fluctuations generated by the interaction of a slow acoustic wave, a fast acoustic wave, and a vorticity wave with distributed roughness for the Case 6. $x_0=200$ mm, $h=0.10$ mm $w=1.25$ mm, $N=40$, $F=1.5*10^{-4}$.

Figure 21. Wall pressure fluctuations generated by the interaction of a slow acoustic wave, a fast acoustic wave, and a vorticity wave with distributed roughness for the Case 7. $x_0=300$ mm $h=0.10$ mm $w=1.25$ mm, $N=40$, $F=1.5*10^{-4}$.
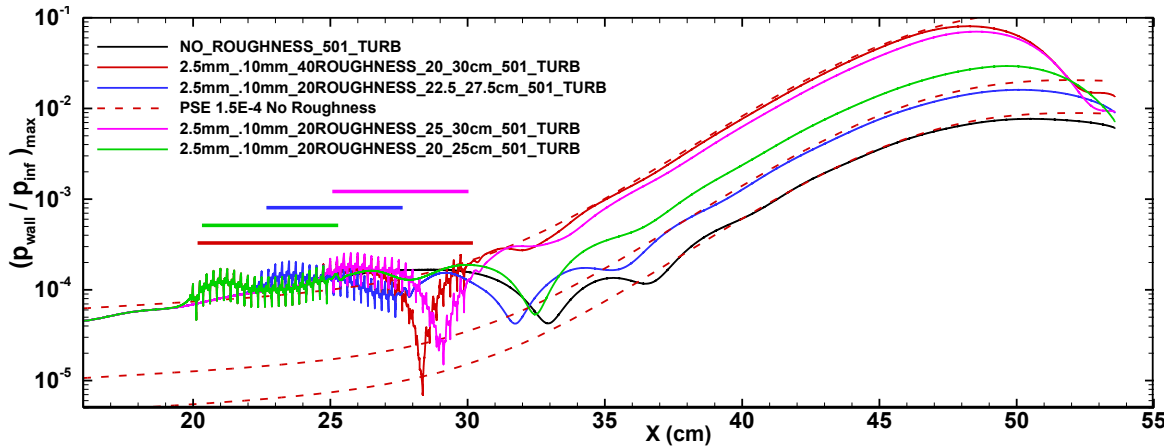
Figure 22. Comparisons of wall pressure fluctuations generated by the interaction of a vorticity wave with distributed roughness for the Cases 6, 9, 10 and 11: (1) no roughness, (2) $x_0=200$ mm, $N=40$, (3) $x_0=225$ mm, $N=20$, and (4) $x_0=250$ mm, $N=20$. $h=0.10$ mm $w=1.25$ mm, $F=1.5*10^{-4}$.
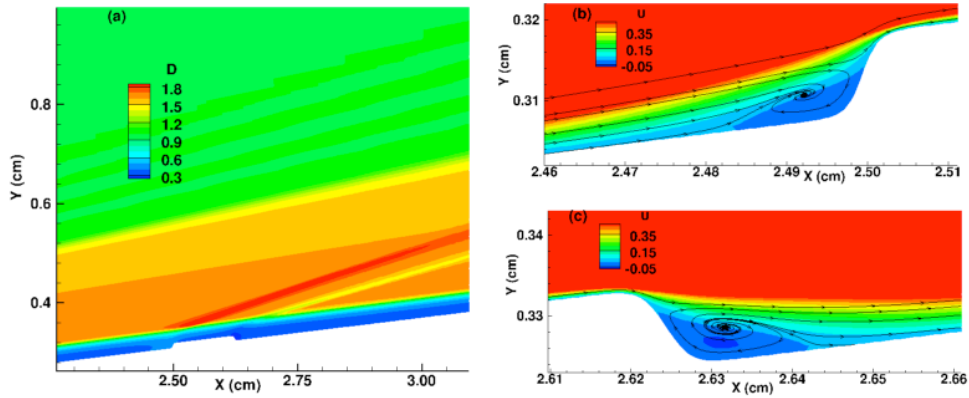
Figure 23. Mean density and velocity contours in the symmetry plane θ=0 with an isolated three-dimensional roughness. (a) density contours, (b) U velocity contours and the streamlines near the leading edge of the roughness, and (c) U velocity and streamlines near the trailing edge of the roughness. h=0.10 mm, $m = 16$, $x_0 = 25$ mm, $\theta_0 = \pi/2$m.
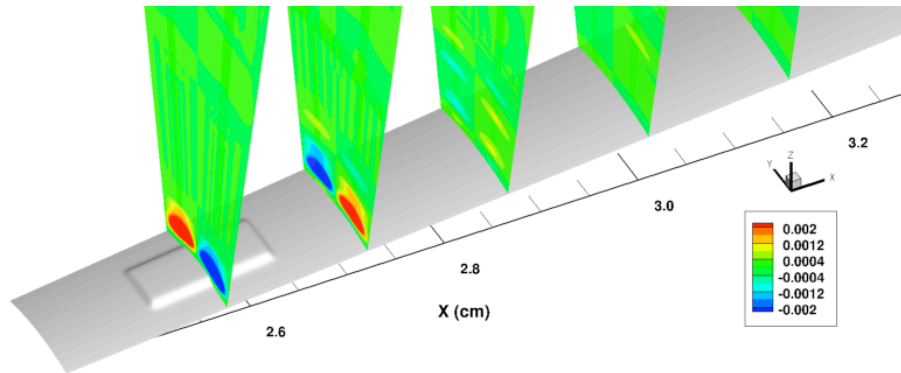

Figure 24. Mean azimuthal velocity contours at different cross sectional (y, θ) planes, x = 2.56, 2.76, 2.96 and 3.16 cm generated by an isolated three-dimensional roughness. h=0.10 mm, $m = 16$, $x_0 = 25$ mm, $\theta_0 = \pi/2$m.
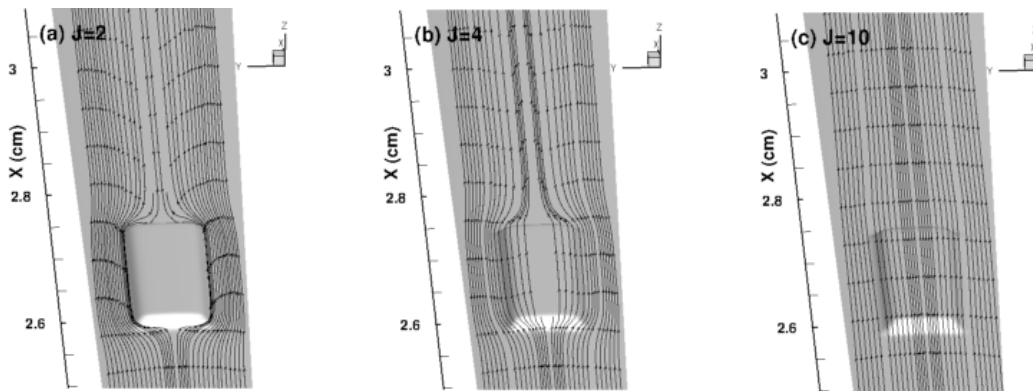
Figure 25. The streamlines over the roughness are shown at different heights in the boundary layer. (a) very close to the surface $y_n = 0.01$ mm, (b) $y_n = 0.02$ mm, and (c) $y_n = 0.10$ mm. The roughness height is 0.10 mm.
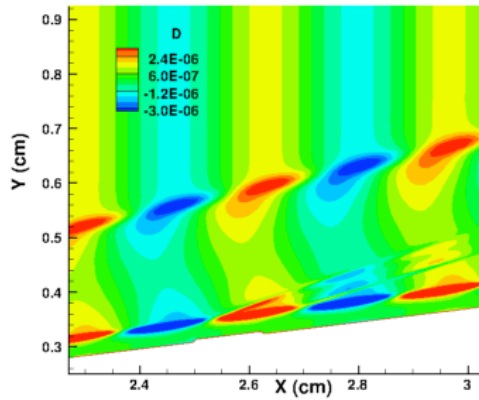
Figure 26. Contours of the density fluctuations generated by the interaction of a slow wave with an isolated roughness in the (x-y) plane along the symmetry plane. $x_0 = 25$ *mm, h=0.05 mm, w=1.25 mm, N=1, F=1.5*10^{-4}.*

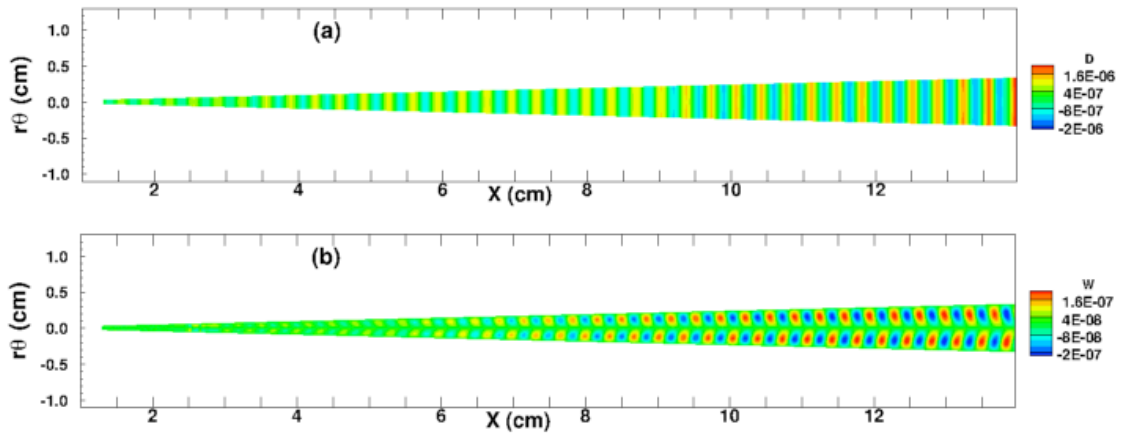**Figure 27. Contours of the (a) density and (b) azimuthal velocity perturbations generated by the roughness and the slow acoustic waves in (x-rθ) plane across the middle of the boundary layer.**

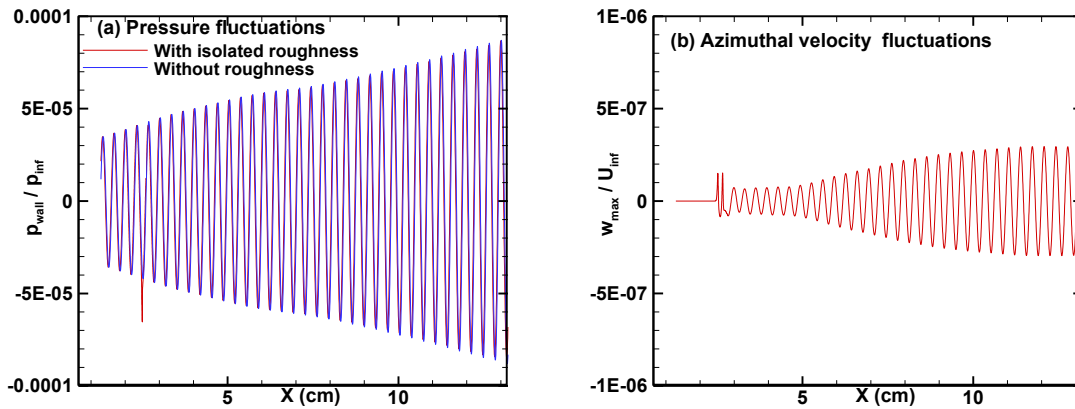**Figure 28. (a) Wall pressure fluctuations and (b) maximum azimuthal velocity fluctuations generated by the roughness and the slow acoustic waves.**
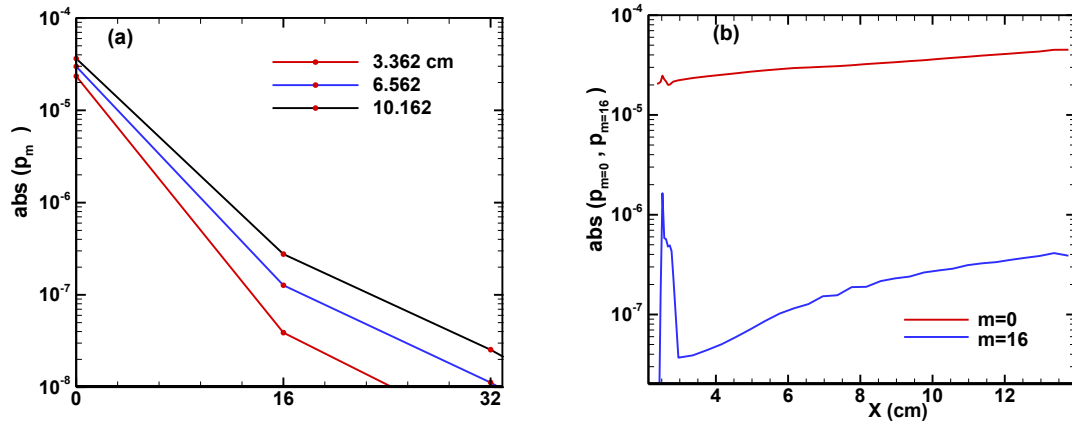
Figure 29. (a) Amplitude of the spectrum of the wall pressure fluctuations at several axial stations and (b) variation of the spectral amplitude for the modes *m*=0 and 16.